Scientific Reports
https://doi.org/10.1038/s41598-026-37117-6

Article in Press

Influence of laser beam intensity profile on deep bone ablation in laser osteotomy

Received: 16 October 2025
Accepted: 19 January 2026
Published online: 03 February 2026

Cite this article as: Liu M., Hamidi A., Blaser D. *et al.* Influence of laser beam intensity profile on deep bone ablation in laser osteotomy. *Sci Rep* (2026). https://doi.org/10.1038/s41598-026-37117-6

Mingyi Liu, Arsham Hamidi, Dunia Blaser, Darren Wilson, Kenneth Garcia, Niklaus F. Friederich, Georg Rauter, Philippe C. Cattin & Ferda Canbaz

Influence of Laser Beam Intensity Profile on Deep Bone Ablation in Laser Osteotomy

Mingyi Liu[1,*], Arsham Hamidi[1], Dunia Blaser[1], Darren Wilson[2], Kenneth Garcia[3], Niklaus F. Friederich[4], Georg Rauter[5], Philippe C. Cattin[6], and Ferda Canbaz[1,*]

[1]Center for Intelligent Optics (CIO), Department of Biomedical Engineering, University of Basel, CH-4123 Allschwil, Switzerland
[2]Smith and Nephew, Registered in England and Wales No.605496 with registered office at PO Box 81, 101 Hessle Road, Hull HU3 2BN
[3]Smith and Nephew Schweiz AG, Theilerstrasse 1A, 6300 Zug, Switzerland
[4]Center of Biomechanics and Biocalorimetry (COB), Department of Biomedical Engineering, University of Basel, CH-4123 Allschwil, Switzerland
[5]Bio-Inspired RObots for MEDicine Laboratory (BIROMED-Lab), Department of Biomedical Engineering, University of Basel, CH-4123 Allschwil, Switzerland
[6]Center for medical Image Analysis & Navigation (CIAN), Department of Biomedical Engineering, University of Basel, CH-4123 Allschwil, Switzerland
[*]mingyi.liu@unibas.ch
[*]ferda.canbaz@unibas.ch

ABSTRACT

Laser osteotomy offers high precision and contact-free bone cutting but remains limited by slower cutting speeds and shallower ablation depths compared to mechanical tools. In this study, we systematically investigated the influence of spatial beam intensity distribution on bone ablation performance by comparing Er:YAG laser with tophat and Gaussian intensity distribution under identical operating conditions. Using bovine femur cortical bone and optimized water–air cooling, the tophat intensity distribution achieved a maximum ablation depth of $44.51\,\mathrm{mm}$ and a maximum average material removal rate of $0.42\,\mathrm{mm^3/s}$, outperforming the Gaussian intensity distribution ($26.51\,\mathrm{mm}$, $0.24\,\mathrm{mm^3/s}$). In dry surface ablation, the tophat profile reached $1.58\,\mathrm{mm^3/s} \pm 0.04\,\mathrm{mm^3/s}$, though with increased carbonization. Compared to previously reported Er:YAG outcomes under optimized ablation conditions, the cutting depth achieved in this work represents more than a twofold improvement, bringing performance close to the planar cut dimensions required during distal femur resurfacing of a total knee arthroplasty (TKA). Scanning electron microscopy and Raman analyzes confirmed minimal compositional change after laser ablation, indicating minimal thermal damage. A steady-state model was utilized to characterize the ablation process and determine the theoretical maximum ablation depth. These findings demonstrate clear ex vivo improvements by using a tophat profile in Er:YAG systems, which have the potential for clinical adoption.

Keywords: laser-tissue interactions, laser ablation, tophat intensity distribution, Gaussian intensity distribution

Introduction

Osteotomy (*oste*= bone, *tomy*= cut) has a rich history, evolving from early civilizations to the era of modern precision surgery. Despite significant advancements in medical technology, the fundamental principle of bone cutting has remained unchanged, such as applying mechanical pressure and friction. Conventional tools such as oscillating and reciprocating saws, rotary burrs and drills, and osteotomes are still routinely used in bone surgery due to their reliability and ease of use[1]. However, these tools can introduce substantial mechanical and thermal stresses into the bone, often resulting in irreversible tissue damage. Due to these induced thermal and mechanical stresses, bone debris is smeared on bone surfaces and patient recovery times are prolonged[2,3]. With an increasing demand for less invasive procedures and faster recovery, both patients and surgeons are seeking advanced surgical techniques that reduce trauma and accelerate recovery. Consequently, alternative methods have been actively explored to overcome the limitations of traditional mechanical osteotomy and improve clinical outcomes in orthopedic surgeries.

In recent years, a growing amount of research challenges conventional osteotomy methods by demonstrating that contact-free modalities can achieve comparable or superior precision while decreasing thermal and mechanical damage[4]. Emerging technologies such as piezoelectric systems[5–7], water jet devices[8,9], and lasers[3,10,11] have been developed to address the limitations of mechanical tools in osteotomy. Among these technologies, the unique features of laser technology, though not recently introduced, continue to offer distinct advantages, including non-contact operation, high precision, reduced collateral damage, and the ability to create customized cutting geometries[10,12,13]. Since its first application in bone cutting[14], laser osteotomy has been subject to extensive research to adapt and optimize laser parameters for orthopedic surgeries. Furthermore, the light-based nature of laser facilitates integration with optical feedback systems, enhancing both safety and precision of laser procedures beyond those achievable with manual surgical techniques[15–18].

Bone tissue consists of approximately 65–70 % hydroxyapatite, 20–25 % collagen, and 10–15 % water[19], therefore, mid-infrared wavelengths are particularly effective for bone ablation, as both water and hydroxyapatite absorb strongly in this range[10]. When irradiated, once the laser energy density exceeds the laser ablation threshold, which is defined as the minimum laser energy density required to initiate material removal, melting, decomposition, spattering, or vaporization, initiate photothermal ablation that removes hard tissue. Several lasers have been evaluated for bone ablation, including CO_2, Er:YAG, and Ho:YAG lasers, each operating at wavelengths that target specific absorption bands of water and hydroxyapatite. Additionally, ultrashort- or nanosecond-pulsed lasers, such as Yb:glass (with a Yb:KYW disk amplifier system)[20], CO_2[21], and Nd:YAG lasers[22] have also been investigated for their ability to minimize thermal effects and reduce dependence on wavelength-specific absorption[23]. In laser–tissue interactions, residual heat that remains in the tissue after removal of the material can cause thermal damage. Depending on temperature and duration, this damage can be reversible or irreversible. Reversible thermal effects involve temporary changes, such as tissue desiccation, while irreversible effects occur when the temperature is sufficiently high to cause permanent damage to the tissue[24]. The thermal damage zone is defined as the region of irreversible thermal injury surrounding the ablation crater. This zone is associated with permanent tissue alterations, including cellular necrosis and cell death. Histological evaluation of bone tissue has shown that after irradiation with pulsed mid-infrared lasers, using microsecond or nanosecond pulse durations, viable osteocytes can still be observed in close proximity to the cutting edge[12,21,25,26]. This indicates that the thermal damage zone is confined to a narrow region adjacent to the ablation area.

Despite advances in laser osteotomy, the prolonged procedure time and limited cutting depth compared to mechanical tools remain a major drawback of this technique[10]. Previous studies on TKA report that the bone preparation step using conventional tools such as the saw blade typically takes between 10 min to 17 min, and an average working time of 15 min. Based on current estimates of the amount of removed bone, the bone removal rate during TKA is approximately 11 mm^3/s[27–31]. The maximum cutting depth required for TKA is approximately 70 mm[28]. However, the bone removal rate and depth achieved with laser osteotomy remains far below that of conventional tools. Ran, T. et al. demonstrated the application of CO_2 lasers in TKA, where simulated five-box cuts on distal ovine femurs were completed in approximately 1.5 h[32,33] and the average removal rate is around 0.30 mm^3/s. However, conventional mechanical tools complete the bone preparation part in about 15 min, highlighting that the cutting speed[34] is a major barrier to clinical adoption. The Ho:YAG laser, with an operating wavelength of around 2.1 µm, shows promise due to the high absorption of water at this wavelength. A recent study reported that with optimized water cooling, the Ho:YAG laser can achieve a maximum ablation depth of 4 mm[35]. Similarly, an ultrashort pulsed Yb-doped fiber laser has a pulse duration of 10 ps, and offers exceptional precision and minimal collateral damage, making it a strong candidate for high-precision bone surgeries; however, the ablation rate and ablation depth of ultrashort pulsed lasers have recently been reported to be 0.18 mm^3/s and 2.8 mm, respectively[36]. The ablation rate in another Yb:KGW ultrafast laser with a pulse duration of 250 fs reached 0.99 mm^3/s without obvious thermal damage, which is about 19 times higher than the previously reported results[37]. Representative parameters of different laser systems used for osteotomy, including wavelength, maximum ablation depth, pulse duration, and removal rate, are summarized in Table 1.

Laser type	Wavelength [µm]	Max depth [mm]	Pulse duration	Removal rate [mm^3/s]
Er:YAG[38]	∼2.94	≈21	350 µs	≈0.17
Er,Cr:YAG[39]	∼2.78	≈8	140 µs	≈0.40
Ho:YAG[35,40]	∼2.10	≈4	600 µs	≈0.94
Yb-doped fiber[36]	∼1.064	≈2.8	10 ps	≈0.18
Yb:KGW[37]	∼1.030	≈1.5	250 fs	≈0.99
CO_2[32]	∼9.3	≈20	25 µs	≈0.50

Table 1. Selected laser systems for laser osteotomy, focusing on maximum depth and ablation rate.

The type of laser-tissue interaction between the laser and bone is also an important criterion for laser selection. Femtosecond and picosecond lasers mainly cause plasma-induced ablation with very low thermal damage, but their ablation efficiency is low for bone. Millisecond or continuous-wave lasers, including CO_2 lasers, induce thermal diffusion and making thermal damage difficult to control. Near-infrared lasers such as Yb:KGW show weak absorption in bone and tend to cause heating rather than efficient ablation. In contrast, microsecond-pulsed lasers lead to efficient ablation with a more controllable thermal interaction[23]. Based on these mechanisms, in laser osteotomy field, we prioritize lasers that can achieve deep ablation and high removal rates with controllable thermal damage. Therefore, compared to other laser types used for bone ablation, such as CO_2, Ho:YAG, and ultrafast lasers, the Er:YAG laser offers a favorable balance between tissue removal efficiency and thermal safety. Er:YAG lasers, operating at 2.94 µm, have been extensively validated for hard-tissue surgery due to their strong absorption in bone constituents and their ability to achieve high-precision ablation with minimal collateral damage. Microscopic evaluations have revealed that the zone of laser influence is extremely narrow, with adjacent bone tissue retaining normal microstructure and viable cells, confirming preservation of a healthy biological environment[41]. Early comparative studies showed that Er:YAG laser osteotomies produced cuts with mechanical integrity equivalent to bur-drilled sites, but with reduced microcracking and negligible carbonization at the interface[42–44]. Optimized cooling protocols have enabled ablation depths of up to 21 mm in bovine femur models[38]. Furthermore, viable osteocytes have been observed near to the resection edge, indicating preservation of biological tissue and supporting improved healing dynamics[45]. In vivo animal studies, particularly in leporine and ovine models, have demonstrated improved bone regeneration and osseointegration following Er:YAG osteotomy compared to conventional drilling[3]. These improvements are attributed to the non-contact, vibration-free nature of the laser and its precise energy confinement. The clinical translation of this technology has been exemplified by the development of the CARLO® (Cold Ablation Robot-guided Laser Osteotome) system by Advanced Osteotomy Tools (AOT, Basel, Switzerland). This robotic, image-guided platform integrated an Er:YAG laser mounted onto a seven-axis robotic arm end-effector to perform precise, contactless bone cuts. In a first-in-human clinical feasibility trial, CARLO® successfully completed 28 osteotomies in the midface and mandible without the need to revert to mechanical tools[46]. The system achieved cutting accuracy within 1 mm root-mean-square deviation, without intraoperative complications and normal postoperative healing, validating the potential of robotic Er:YAG laser osteotomy in clinical practice[47].

Until today, mainly laser wavelength and irrigation conditions have been analyzed in order to increase ablation depth and material removal rate. Another method to increase ablation depth that has not yet been systematically analyzed is beam shaping. Although beam shaping is an established optical approach, its systematic application to deep bone ablation has been limited. This study provides a direct comparison of maximum ablation depth under otherwise identical conditions. In our experiments, the maximum ablation depths were 44.51 mm using the tophat and 26.51 mm using a Gaussian intensity distribution. The ablation process and theoretical maximum ablation depths were investigated using a steady-state model informed by empirical surface ablation rate measurements, enabling the determination of maximum depth under current experimental conditions. Furthermore, under identical conditions, the tophat intensity distribution achieved approximately 1.7 times the ablation depth and roughly twice the material removal rate in comparison with that of the Gaussian intensity distribution, whilst causing less thermal damage to surrounding tissue. To the best of our knowledge, these are among the deepest ex vivo ablation depths reported with Er:YAG lasers under water-assisted conditions. The tophat intensity distribution, when combined with water and air, achieved average and surface material removal rates of $0.42\,mm^3/s \pm 0.01\,mm^3/s$ and $0.96\,mm^3/s \pm 0.03\,mm^3/s$, respectively. Although the maximum ablation rate is comparable to that in Ref.[37], the ablation depth is considerably higher, highlighting the clinical potential of the Er:YAG laser with a tophat intensity distribution.

Results

Beam and temporal profile analysis

Figure 1 shows the 3D and top views of tophat and Gaussian intensity distributions. The beam profiles were collected at 600 mJ and 650 mJ output energy levels, and at 750 mm and 1250 mm distances from the lasers with the tophat and with Gaussian intensity distributions, respectively. The full-angle divergence was 12.8 mrad for the tophat and 7.7 mrad for the Gaussian beam. The measured tophat intensity distribution is almost uniform with small fluctuations (as can be seen in Figure 1a), whereas Figure 1b clearly delineates the sidelobes of the laser with Gaussian intensity distribution, corresponding to highly multimode laser output. These sidelobes usually do not contribute to the ablation process. However, the energy carried causes a temperature rise in the surrounding tissues, which can increase the risk of thermal necrosis. In this study, to simplify the description of Gaussian beams, we use the term ‘Gaussian intensity distribution’ to refer to ‘multimode Gaussian intensity distribution’. In addition, the Rayleigh length after the second lens is 22.8 mm for the tophat intensity distribution and 31.7 mm for the Gaussian intensity distribution. The detailed description of the experimental setup can be found in the "*Experimental setup*" section in "*Methods*".

The temporal pulse profiles of the tophat and Gaussian intensity distribution were measured using a photo detector (PDA20H, Thorlabs). All measurements were performed under identical operating conditions, with a repetition rate of 10 Hz and a pulse energy of 600 mJ. As shown in Figure 2, both laser systems exhibit stable pulse trains with a pulse interval of 100 ms. The corresponding single-pulse temporal profiles reveal pulse durations of approximately 500 µs for both beams. Despite the similar operating parameters, slight differences in the temporal pulse shapes are observed between the tophat and Gaussian beams. These differences are likely attributable to variations in laser architecture.

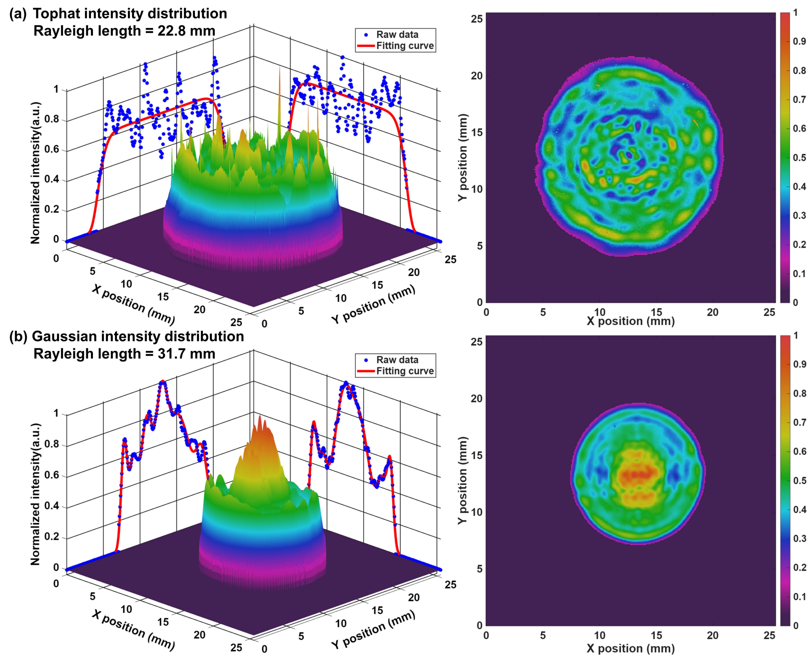

Figure 1. Beam profile of (a) tophat intensity distribution and (b) Gaussian intensity distribution at 600 mJ and 650 mJ output power, respectively. The beam profiles were measured at 750 mm and 1250 mm distances from the respective laser; the beam was reflected to these positions by an optical window to reduce the laser fluence on the beam profiler. (Note: Due to the difference in beam divergence angle of two intensity distributions, different distances were used to completely separate the beam spots avoiding interference in the beam profile measurement.)

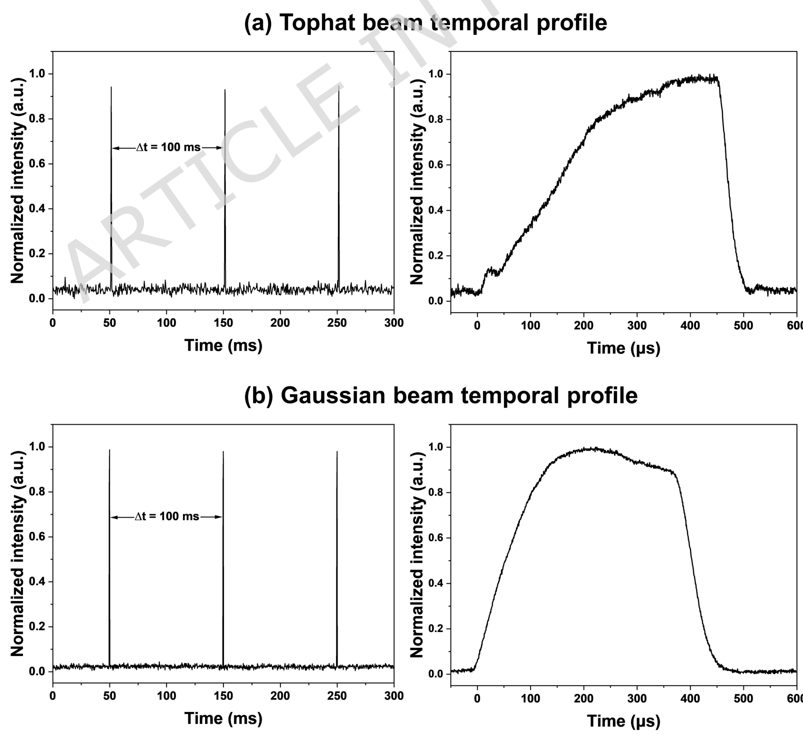

Figure 2. Pulse trains and temporal profiles of (a) tophat and (b) Gaussian intensity distribution.

Material removal rate evaluation

Figure 3 shows the comparison of material removal rate under three conditions: (1) dry ablation, also known as direct ablation (without water irrigation and compressed air); (2) water irrigation only for cooling; and (3) a combination of water irrigation and compressed air to remove both debris and excess water while supporting surface cooling. As can be seen in Figure 3, under all the tested conditions, the material removal rate for both types of beam profiles exhibited a saturation trend as fluence increases. At approximately 100 J/cm^2, corresponding to a laser pulse energy of around 1.2 J, the material removal rate gradually approached a constant value. This suggests that a further increase in output energy would not significantly enhance the removal rate. Therefore, 1.2 J/pulse was selected as a reasonable energy for further ablation experiments.

The maximum surface material removal rate for dry ablation using the laser with tophat intensity distribution reached 1.58 mm^3/s$\pm$0.04 mm^3/s. Under the same conditions, the laser with Gaussian intensity distribution achieved approximately half this rate around 0.78 mm^3/s$\pm$0.04 mm^3/s. In other tested conditions (water irrigation and water irrigation combined with pressurized air), the material removal rate of the laser with tophat intensity distribution was consistently about twice that of the Gaussian one. We performed the ablation rate experiments under the same experimental conditions to have a consistent comparison. Based on the material removal rate results, we can conclude that, at the same fluence, the tophat is more energy-efficient than the Gaussian and can remove material faster. This also supports the subsequent ablation results, where the tophat can achieve deeper ablation at the same fluence level. Experimental details can be found at "*Material removal rate evaluation*" section in "*Methods*")

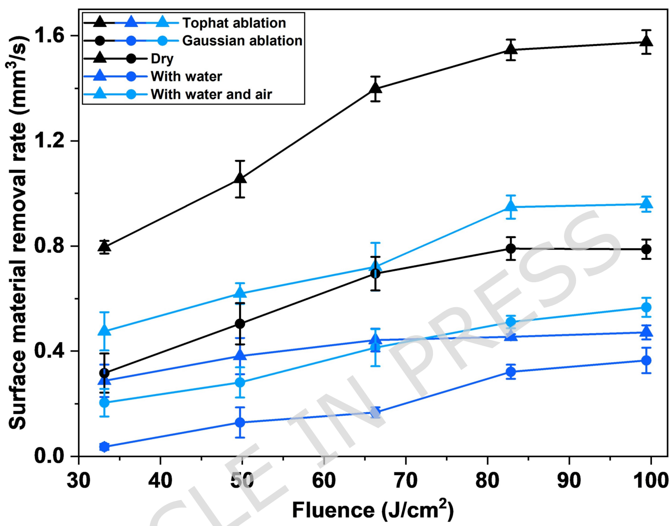

Figure 3. Comparison of the surface material removal rates of lasers with tophat and Gaussian intensity distribution at three different ablation conditions: dry, with water, and with water and air. The error bars show the standard deviation. Each data point represents the mean value from six ablation lines (three samples, two lines per sample).

Ablation parameter investigation

In the ablation experiments, the focal length of the focusing lens and the sample position relative to the lens determine the initial laser fluence on the sample surface. A straightforward strategy is to position the sample at the focal plane to maximize fluence, or at a distance of $-Z_R$ (to efficiently use the entire depth of focus) from the focal plane to maintain a constant fluence over the full depth of focus.

Our experiments indicated that sample placement strongly affects the achievable maximum ablation depth. Therefore, in the subsequent tests using the beam with the tophat intensity profile, we systematically positioned the sample at various points before and after the focal plane to identify the optimal configuration while maintaining a constant water pressure of 5.5 bar. Before optimizing the lens-to-sample distance, we first tested different lenses with different focal lengths for the second lens. These two lenses were selected because they result in almost identical beamwaist radius which is shown in Table 2. The ablation results showed that a focal length of 100 mm provided the best depth performance for the tophat intensity distribution, while a focal length of 150 mm was optimal for the Gaussian intensity distribution. These lenses were selected as fixed conditions for the following optimization.

As shown in Figure 4a, placing the sample about 91 mm from the second lens (focal length, f = 100 mm) resulted in an ablation depth of 37.25 mm$\pm$0.25 mm, with an ablation time of approximately 11 min. At this position, the focal plane is $\sim$10 mm below the surface, corresponding to 1/2 of the Rayleigh length that traverses the sample.

Initially, the water pressure was adjusted to a safe level at 5.5 bar considering the requirements in an operating room[48]. However, all of the ablation experiments showed traces of carbonization at the deepest points, suggesting that the water jet was unable to reach the deepest point in the cut. After distance optimization experiments, we varied the water jet pressure from

5.5 bar to 30 bar. At a water pressure of 15 bar, we achieved a maximum ablation depth of approximately 43.75 mm±0.51 mm in 11 min. Based on the literature, the minimum water pressure for bone cutting using water is 50 MPa (500 bar)[49]. We did not observe any damage due to the applied water pressure at 15 bar.

Based on the results with the tophat intensity distribution, we applied the same conditions for ablation to the laser with Gaussian intensity distribution, using a water pressure of 15 bar to investigate the relationship between sample distance and ablation depth. We changed the focusing lens in the laser with Gaussian intensity distribution ablation case to reach the same fluence level on the sample. As shown in Figure 4a, when the sample was placed at 165 mm distance from the second lens (f = 150 mm), the depth obtained was 26.14 mm±0.36 mm in 11 min.

In a separate experiment, we applied pulsed water irrigation to control the amount of water on the surface during ablation experiments. The on/off intervals were also determined based on the depth yield. Pulsed water with intervals of 5 s, 10 s, 20 s, 30 s, and 40 s was tested to cool the samples, and the total duration of the experiments was 10 min and 30 s. The corresponding micro-CT images are shown in Figure 4b. A pulsed water interval of 30 s yielded the ablation depth of 44.10 mm±0.27 mm, with the corresponding average material removal rate of 0.42 mm^3/s±0.002 mm^3/s. A 30 s water pulse interval also offered the highest ablation efficiency. Therefore, this condition was used in all subsequent experiments.

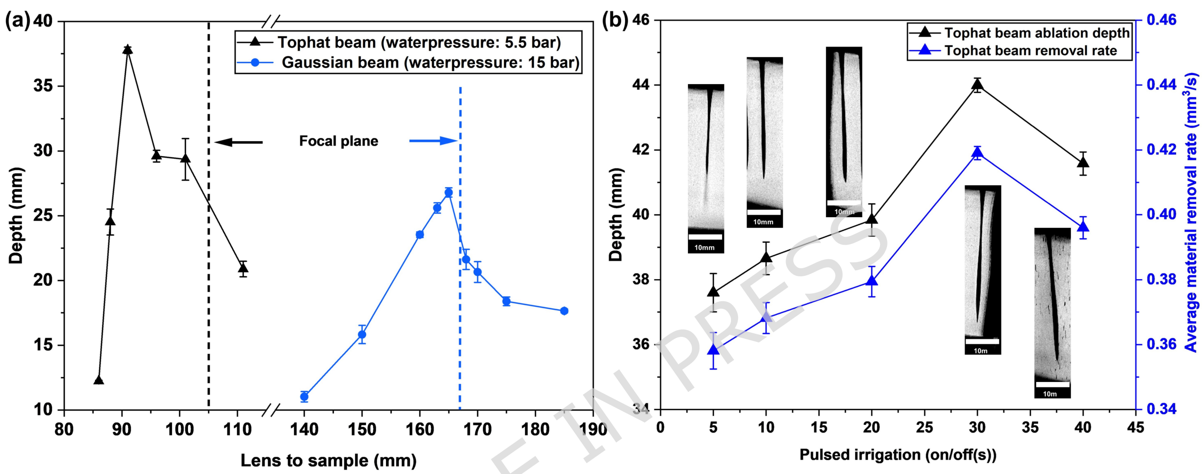

Figure 4. Ablation parameter investigation to optimize the ablation depth. (a) Maximum ablation depth as a function of the distance from the lens to the sample using tophat and Gaussian beams. (b) Testing various intervals for pulsed water irrigation (Laser: tophat intensity distribution, water pressure: 15 bar). The error bars show the standard deviation. Each data point represents the mean value from three ablation lines on one sample.

Beam profile along the depth of ablation

To investigate how the tophat and Gaussian intensity distributions affect the ablation depth using the same setup configuration (water irrigation interval and compressed air pressure), we conducted a comparative experiment (a detailed setup is shown in "*Experimental setup*" subsection in "*Methods*"). During ablation, all the optimized parameters based on results in the "*Ablation parameter investigation*" section were applied for both lasers. These ablation parameters were as follows: water with a water pressure of 15 bar at an interval of 30 s during the experiments.

To obtain accurate measurements, the samples were scanned using a Micro-CT system (GE nanotom m, Phoenix) with a resolution of 40 µm after ablation (Specifications can be found in the "*Depth measurements and bone analysis*" section in "*Methods*"). The results showed that the Gaussian intensity distribution achieved an ablation depth of approximately 27.3 mm, while the laser with the tophat intensity distribution reached 43.8 mm, which is $\sim$1.6 times deeper. The CT images reveal a V-shaped ablation profile for the Gaussian beam, while the cross-section of the tophat ablation clearly shows the overlap with the propagation profile of the beam. As shown in Figure 5a, the laser with the tophat intensity distribution was focused until it reached the focal plane. After reaching the narrowest point near the focal plane, it diverged again within the sample.

To further analyze these results, we acquired the beam profiles along the laser propagation path using the beam profiler (PY-IV-C-A-PRO, Ophiropt). This was achieved by systematically scanning the profiler, starting at a position of 10 mm before the focal plane, and obtaining the beam profile every 2 mm steps. The beam profiles of the tophat intensity distribution and the Gaussian intensity distribution were measured under 583 mJ and 572 mJ output power, respectively. In the experiments, we measured the focal plane distances from the lenses to be approximately 105 mm and 168 mm for the tophat and the Gaussian intensity distributions, respectively. The discrepancy between the focal lengths of the lenses and the measured focal distances is possibly due to the difference between the design wavelength of the lenses (588 nm), the laser wavelength and the M^2 factors of the Er:YAG lasers. Figure 5a and Figure 5b show changes in the beam profiles as a function of the distance from the lens. The full-width at half-maximum (FWHM) and the corresponding ablation widths were calculated for both laser types along the propagation axis. As shown in Figure 5c and Figure 5d, for the tophat intensity distribution, the ratio between the ablation width and the beam FWHM continuously decreased before the focal plane and increased again after passing the focal plane. In contrast, for the Gaussian intensity distribution, this ratio continuously decreased during propagation.

At each position, the spatial beam profile was integrated to determine the energy delivered, from which the ablation energy efficiency was calculated, assuming that the beam profiles will remain similar at higher energy levels of both lasers and propagating within the walls of the cut. Figure 5c and Figure 5d show that the tophat intensity distribution achieved 98% energy efficiency on the sample surface, indicating that most of the energy contributed to ablation. The energy efficiency decreased with distance until near the focal plane, and then increased again to above 90%, indicating that the clipping losses were minimized. As the ablation distance is increased, the fluence is reduced due to the augmentation in beam size, eventually diminishing to approximately 10% efficiency. Figure 5b shows the V-shaped ablation crater. For the Gaussian beam, the initial energy efficiency was above 90%, then it decreased to as low as 10% at the bottom of the cut. In the case of the Gaussian beam, only a restricted portion of the beam contributed to ablation. As the ablation depth increased, the effective width of the cut decreased, which caused an aperture effect and wasted the laser energy, limiting the ablation depth. However, for the laser with tophat intensity distribution, although the energy efficiency decreases to the lowest level at the focal plane, it recovers after the focal plane, then starts decreasing only after the beam diameter is large in a deeper point of the cut, thus enabling deeper ablation. Overall, under identical laser parameters and cooling conditions, the tophat intensity distribution delivered higher energy to deeper points in the cut and overcame the aperture effect limitations seen with Gaussian beams.

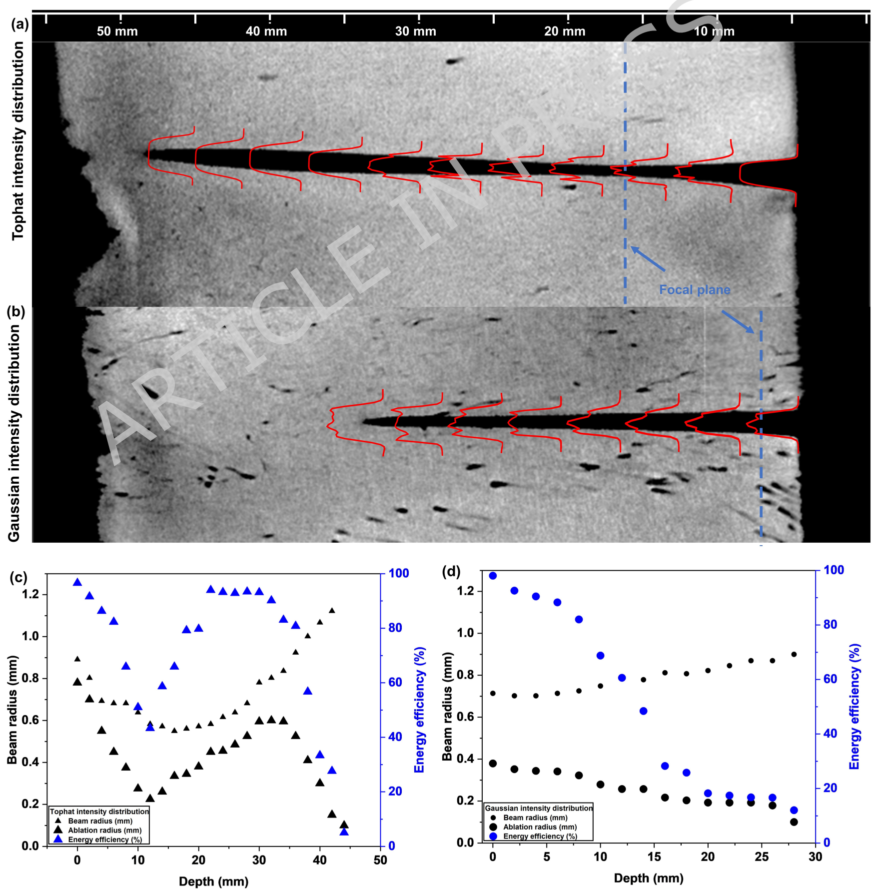

Figure 5. Ablation profile obtained using laser with (a) tophat and (b) Gaussian intensity distribution. The measured beam profiles of both lasers are also shown on the ablation profile with red curves. The scale of the CT scan and beam profile measurements are adjusted to be the same. Variation of beam size, crater size, and energy efficiency are shown in (c) tophat and (d) Gaussian intensity distribution.

Ablation evolution

Achieving deep ablation with minimal carbonization remains a key challenge in bone ablation research. Improving both the removal rate and depth of ablation is always a central focus in the field. This study explored deep-ablation experimental parameters using two beam profiles. All parameters can be found in the "*Ablation parameter investigation*" section below. The experimental setup details are provided in "*Experimental setup*" section in "*Methods*".

We ablated five times on each sample using the same ablation parameters. To accurately measure the depth of ablation, Micro-CT scans were performed on the samples (Specifications can be found at "*Depth measurements and bone analysis*" section in "*Methods*"). The corresponding results are shown in Figure 6a. To better visualize the shape of the ablation crater cross-section, we used the open source OpenCV library in Python to extract the ablation profile, depicted with the green line next to each enlarged CT scan image in Figure 6a. The results showed that under identical conditions, the laser with the tophat intensity distribution achieved a maximum ablation depth of 44.51 mm and a maximum average material removal rate of 0.42 mm^3/s. The corresponding average values were 43.86 mm$\pm$0.65 mm for ablation depth and 0.40 mm^3/s$\pm$0.006 mm^3/s for material removal rate. In contrast, the Gaussian intensity distribution reached only 26.51 mm and 0.24 mm^3/s, with averages of 26.24 mm$\pm$0.27 mm and 0.24 mm^3/s$\pm$0.004 mm^3/s over a period of 11 min for both beam profiles. The profiles of the ablation craters are also shown in Figure 6a.

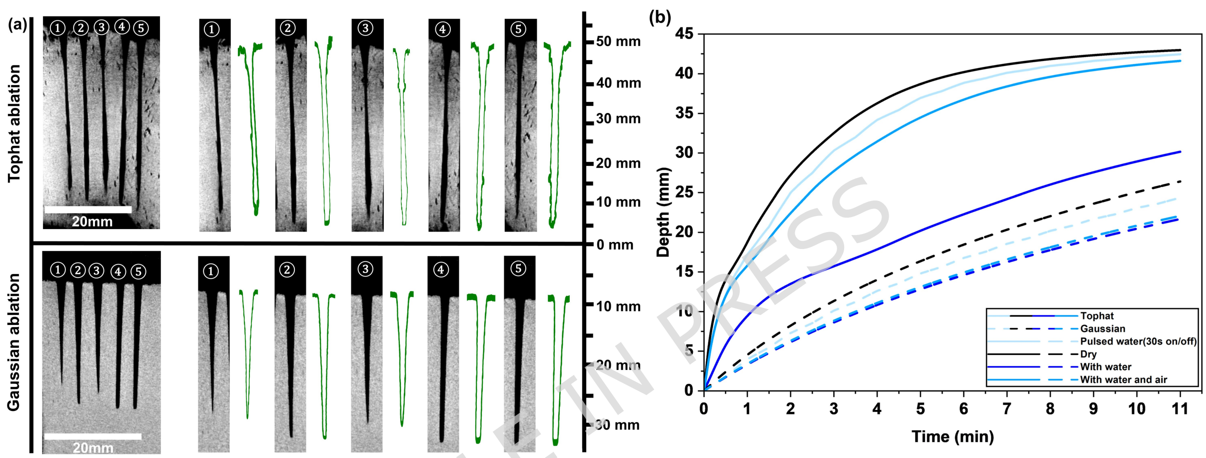

Figure 6. (a) CT scan images of both tophat and Gaussian ablation. The green line is the outline of each ablation crater (b) The expected ablation depths using lasers with tophat and Gaussian intensity distribution based on the measured ablation rates and ablation conditions.

To better understand the ablation process and the theoretical maximum ablation depth, we used the steady-state model[23]. The depth variation data are extracted from the surface ablation rate measurements shown in Figure 3. The maximum ablation depth under the current conditions was obtained through this modeling approach (for detailed modeling theory, please refer to the "*Theoretical modeling of the ablation process*" section in *Methods*).

In the model, we included dry ablation, with water, and with water and air conditions, and also mimicked the real experimental condition of pulsed water irrigation, which was changed every 30 s in the model. The model alternated between dry ablation and water and air conditions by using the corresponding ablation rates accordingly after every 30 s. Since the experiments began with the condition, ablation with water and air, the model used the corresponding ablation depth for the initial pulse.

As shown in Figure 6b, lasers with tophat and Gaussian intensity distribution under ablation with pulsed water irrigation conditions, the expected maximum ablation depths are above 43.3 mm and 25.2 mm in 11 min, respectively. These values follow the experimental observations. However, the model uses simplified assumptions about the material and heat processes, and cannot fully represent the complex conditions of real life experiments. Hence, the simulated ablation results are slightly lower than the experimental results. In the future, a more accurate model can be developed by simulating more experimental processes, including debris interactions, which may lead to more precise model results and provide better guidance for optimizing real experiments.

Scanning Electron Microscopy analysis

The thermal effects of both beam profiles are also investigated in a separate bovine femur sample. Scanning Electron Microscopy (SEM) analysis (EM30AX, COXEM) was performed to analyze the microstructure of bone samples (for detailed specifications and sample preparation, please refer to the "*Depth measurements and bone analysis*" section in *Methods*).

Within these analyzes, three different sections were studied. The laser beams (tophat and Gaussian) irradiated the samples under the same conditions (ablation with water and air, water pressure at 15 bar, and laser energy of 1.2 J on the sample) as in the deepest ablation experiments.

In Figure 7a and Figure 7b, each SEM image was divided into three analysis regions: ablated area (irradiated by laser beam), healthy bone (base bone), and the interface between these two demarcated regions. As a reference and also for comparison with carbonized samples, we performed hole ablation on a bovine femur sample using the laser with tophat intensity distribution. To induce carbonization, no water cooling was applied during the ablation process. The laser energy on the sample was 1.2 J, with an ablation duration of 2 min. After the ablation process, the sample was dried for 72 h before SEM imaging.

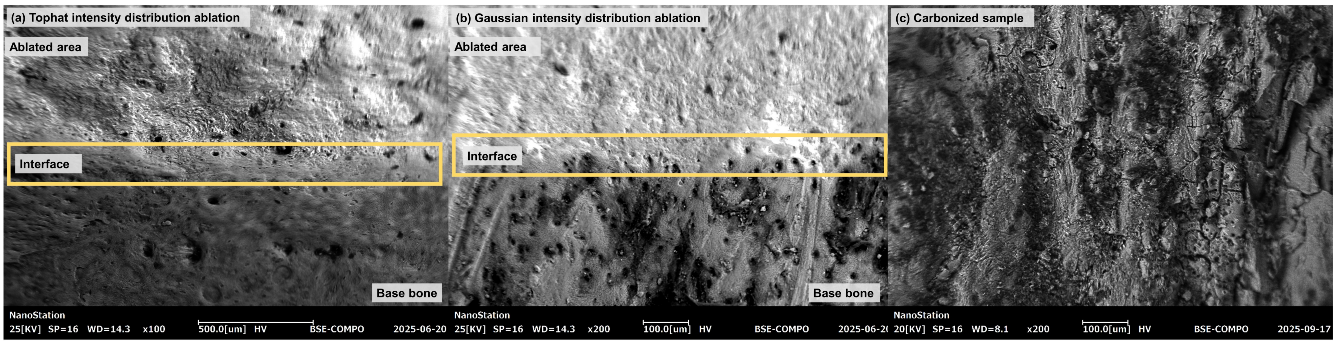

Figure 7. Representative SEM images for Er:YAG lasers ablation with (a) tophat intensity distribution and (b) Gaussian intensity distribution. (c) an SEM image of a carbonized sample to visualize changes in surface structures.

Following laser irradiation, a comprehensive analysis was performed using SEM to evaluate the structural integrity of the bone tissue. A primary focus of this analysis was the preservation of osteocyte lacunae, which are the microscopic voids that house osteocytes. Because these specialized cells, derived from osteoblasts[50–52], form an intricate cellular network essential for the mechanotransduction and regulation of bone remodeling[53]. The integrity of this lacunar-canalicular network is directly correlated with osteocyte viability; its disruption can lead to osteocyte apoptosis[51], which subsequently compromises bone homeostasis and reparative processes. The successful preservation of these microstructures post-ablation is a critical metric for assessing the minimal thermal impact of the procedure, a condition we have designated as healthy ablation.

The SEM images, presented in Figure 7a and Figure 7b, depict bone samples subjected to ablation by a tophat intensity distribution and a Gaussian intensity distribution, respectively. The images demonstrate the structural preservation of the osteocyte lacunae within the interface region, with no discernible signs of thermal damage. The SEM image of the carbonized sample, as shown in Figure 7c, clearly reveals charcoal-like structures which indicate the complete loss of osteocyte lacunae. These observations serve as supportive evidence for the high quality and precision of the ablation process. These findings strongly indicate that water-assisted laser ablation can achieve precise, low-damage tissue removal, even at high power settings and rapid removal rates. This has significant implications for orthopedic surgery, particularly for procedures such as TKA, where maintaining the viability of surrounding bone tissue is paramount for implant integration and long-term clinical success. These SEM observations were qualitative; to measure the precise thermal damage zone in micrometers, future studies with histology and viability staining are required to quantify cell preservation.

Raman Spectroscopy

Raman spectroscopy is a powerful technique that analyzes the vibrational modes of molecules, providing information about the chemical composition and structural changes within bone. Changes in the Raman spectra of ablated bone samples can indicate potential structural damage, such as protein denaturation or carbonization. For bone tissue, hydroxyapatite and organic components are the primary constituents.

In Raman spectral analysis, the main characteristic peaks of healthy (base, native) bone include phosphate bending vibration (δPO_4, 427 cm^{-1} and 585 cm^{-1}), phosphate stretching vibration (νPO_4, 959 cm^{-1}), and carbonate stretching vibration (νCO_3, 1070 cm^{-1})[54]. Therefore, Raman spectroscopy was conducted on both native bone samples (fresh mature bovine femur samples, base bone) and ablated areas of the bone samples (Detailed parameters and testing process are shown in "*Depth measurements and bone analysis*" section in "*Methods*". To compare the effects under different ablation conditions, we tested three ablation conditions: dry ablation, ablation with water, and ablation with both water and compressed air. Raman spectra were also collected from carbonized bone and fresh bone samples as reference measurements.

The results are shown in Figure 8. When comparing the spectra under all ablation conditions with those of the native or base bone, all the fingerprint vibrational modes mentioned above were still present. Due to long data collection and laser exposure times, the water band around 1640 cm^{-1}[55] was weak. Although the intensity of the νPO_4 peak showed a slight decrease after ablation, the characteristic peaks remained intact. In contrast, in the carbonized bone samples, the primary characteristic peaks were absent; only elevated background noise remained. This indicates that no fundamental structural damage occurred in the bone samples following either of the two laser ablation methods as was previously reported[54].

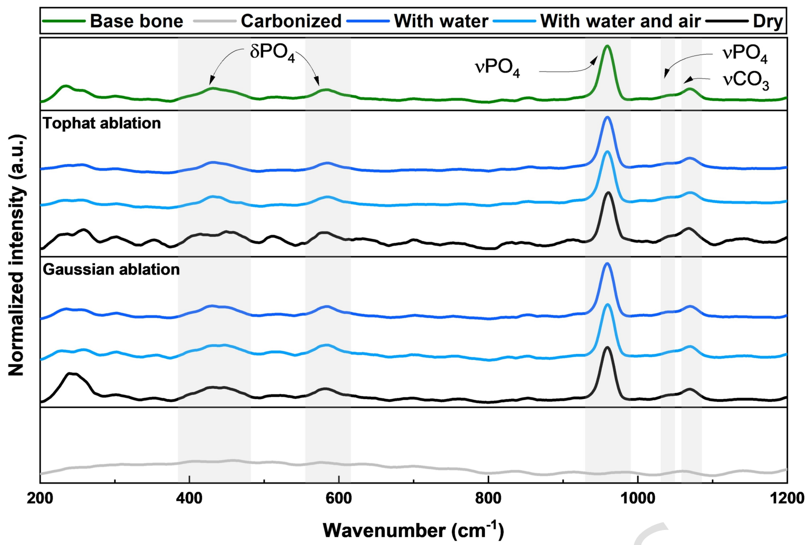

Figure 8. Raman spectra of native (base), carbonized, and ablated bone samples using lasers with tophat and with Gaussian intensity distributions. We introduced an offset to the normalized Raman spectra to increase the visibility of each vibration band. The three ablation conditions were applied to the bone surface to identify the effects of both lasers.

Discussion

This study investigates the effect of the spatial intensity distribution of Er:YAG laser beams on ablation speed and depth. Although our comparison may be limited by using two different beam profiles, the observed performance differences are consistent with theoretical predictions for lasers with tophat and Gaussian intensity distributions. Er:YAG lasers are favorable for bulk ablation, as the literature has repeatedly demonstrated. However, beam shaping in this spectral range remains largely unexplored, likely due to the limited availability of suitable diffractive elements. Traditional Er:YAG lasers typically produce a multimode output closely resembling a Gaussian intensity distribution, characterized by a high central intensity and accompanying sidelobes. This generally results in a conical-shaped ablation profile in bone, caused by spatial filtering of the cut walls as the depth increases. This behavior is clearly visible in Figure 5. In a Gaussian beam, only portion of the beam exceeding the ablation threshold contributes to material removal. Lower intensity peripheral regions are blocked after only a few pulses, leading to a steady decrease in effective fluence with successive pulses. Ablation depth can only increase as long as the central portion maintains sufficient fluence to ablate the bone.

In contrast, a uniform intensity or tophat intensity distribution delivers ablation-capable fluence across its entire cross-section. Especially if the edges of the beam are steep, the resulting ablation profile is expected to have a flat bottom, following the beam profile. The process begins with an average fluence just above the ablation threshold, focuses within the bone, and continues until the average fluence drops below the threshold. Although such a beam might be expected to produce a roughly symmetric depth profile, our experiments showed that the maximum depth is achieved when the focal plane is positioned ~10 mm below the bone surface. When the sample was placed far before the focal plane, the enlarged spot reduced fluence and efficiency with increasing depth, preventing maximum penetration.

The tophat beam yielded its maximum ablation depth of 44.51 mm, at a position of 10 mm before the focal plane. The progression of ablation was initially sustained despite an in-depth decrease in energy efficiency, which corresponded to a reduction in effective fluence. The efficiency subsequently recovered once the beam had passed the focal plane, continuing until the inherent beam expansion limited further cutting capability. The average material removal rate was approximately 0.45 mm^3/s in the upper 22 mm, and 0.40 mm^3/s in the lower 22 mm, different for the two halves. In particular, after reaching the focal plane, the tophat intensity distribution continued to increase depth by an additional ~34 mm, albeit at a slower rate. A possible contributing factor could be mild heat accumulation at the bottom of the cut, allowing localized continuation of ablation even when the surface fluence is low. In the Gaussian case, energy efficiency declined steadily with depth, as sidelobes consistently remained below the ablation threshold and were therefore inactive for cutting. Further depth increase was not achievable.

In addition to these optical and geometric limitations, dynamic interactions between the laser, water, and ablation debris introduce further shielding effects. Shielding effects are also a crucial phenomenon in pulsed laser bone ablation, particularly with microsecond lasers like the Er:YAG, that reduce the effective fluence reaching the tissue and limit the maximum ablation depth[56]. Shielding occurs when ablated material interferes with the incoming laser beam. It is primarily driven by two components: vapor plume/plasma formation and particulate/debris ejection. The rapid absorption of laser energy by water in the tissue causes explosive vaporization, leading to the formation of a high-pressure, high-temperature vapor plume above the target[23,56]. At high laser intensities, this plume can be ionized into a plasma[57]. This plume or plasma strongly absorbs, scatters, or refracts the latter parts of the incident laser pulse, decreasing the energy deposited onto the bone surface. Additionally, the thermo-mechanical ablation process ejects solid bone microparticles, fragments, and water droplets into the beam path. These particles scatter laser light, contributing to the overall loss of effective fluence. The main consequence of shielding is a significant reduction in ablation efficiency, which can be modeled when determining clinical laser dosage[56]. In experiments, the energy deposited into the sample can be reduced by 25% to 50% due to shielding from the ejected material[56]. Mitigation strategies often focus on pulse control and clearing the ablation zone. Using ultrashort-pulsed (ps or fs) lasers can minimize the time for the plume or plasma to form and interfere with the pulse, effectively reducing this shielding mechanism[58]. Employing effective water irrigation or microjet systems also helps mechanically to clear the plume and debris, maximizing the energy delivery of subsequent pulses and improving ablation rates[56,59]. Additionally, liquid layers can enhance ablation by confining the laser-generated plasma, leading to photomechanical effects, although shielding can still cause efficiency saturation at high radiant exposures[57].

Although the tophat intensity profile utilized a shorter focal length lens, resulting in a higher divergence angle than the Gaussian beam, its depth-dependent cut profile varied more slowly. This characteristic effectively avoided the severe efficiency loss observed with the Gaussian intensity distribution. This difference is apparent in CT images Figure 5a and Figure 5b for tophat and Gaussian ablation profiles, respectively.

Under identical parameters (ablation with water and air), when the samples were positioned at the focal plane of both intensity profiles ("*Material removal rate evaluation*" section in "*Results*"), the laser with tophat intensity distribution achieved a maximum surface material removal rate of $0.96\,\mathrm{mm^3/s} \pm 0.03\,\mathrm{mm^3/s}$, about 1.7 times higher than the Gaussian intensity distribution. SEM and Raman spectroscopy analyses indicated that the bone structure remained undamaged after laser ablation. The Raman spectra showed intact phosphate and carbonate peaks, indicating low observable damage under ex vivo conditions. While these techniques are effective in identifying gross thermal or chemical damage, they are inherently qualitative in nature. Therefore, SEM was used to perform a qualitative analysis of osteocyte lacuna–canalicular network preservation to assess thermal damage. Although this approach clearly reveals differences in thermal effects, a quantitative analysis would provide a more objective and detailed evaluation. However, it is difficult to define reliable metrics because natural bone samples do not have a uniform microstructure. Despite this limitation, the performance advantage of the tophat intensity distribution is clearly reflected in the achieved ablation depth. The laser with a tophat intensity distribution achieved a maximum depth of 44.51 mm in approximately 11 min, whereas the laser with a Gaussian intensity distribution reached only 26.51 mm. Compared to previously reported Er:YAG results in cortical bone (maximum depths 21 mm[38] under comparable cooling and scanning conditions), the depth achieved here represents approximately a twofold improvement, approaching the 70 mm ablation depths required by orthopedic applications[28]. This was achieved without increasing pulse fluence, repetition rate, or other ablation parameters, isolating the beam profile as the primary variable.

To further elucidate the physical mechanisms underlying the ablating performance observed in this study, the ablation process and theoretical maximum ablation depth were investigated using a steady-state model informed by empirical surface ablation rate measurements, enabling to determine the maximum depth under current experimental conditions. This theoretical framework provides a link between microscopic optical interactions and macroscopic ablation results. The optical penetration depth (δ) of the Er:YAG laser is calculated at approximately 7.7 µm based on the Beer-Lambert Law and the static absorption coefficient of water ($\mu_a = 13\,000\,\mathrm{cm^{-1}}$)[60], the steady-state analysis suggests that beam geometry is the critical factor in reaching depths exceeding 40 mm. But with respect to multiple pulses and the spatial distribution of laser intensity, the present model is limited to describing single-pulse ablation under the experimental conditions of this study. The effect of multiple pulses is not explicitly included in the model, and the reported ablation depth is obtained by applying the single-pulse ablation result to the experimental conditions. The spatial laser intensity distribution is assumed to be fixed and reproducible. A model explicitly accounting for pulse-to-pulse effects and spatial intensity variations will be addressed in future studies.

These findings represent the promising performance of deep bone laser ablation, narrowing the gap in cutting efficiency with standard mechanical osteotomy tools. With further improvements and integration into robotic delivery systems, Er:YAG lasers with tophat profile have the potential to meet both the speed and depth requirements for orthopedic mainstream surgery.

The following are potential limitations of this study. First, bovine femur samples were obtained from commercial sources of unknown freshness and subjected to freeze–thaw storage, which can alter hydration and microstructure. therefore, absolute ablation values may differ from those of fresh living bone. Second, the comparison relied on two distinct commercial Er:YAG systems, so residual differences in optical design beyond the beam profile may have contributed to the observed effects. Finally, all experiments were conducted ex vivo under controlled irrigation, which does not replicate the physiological environment of perfused, vascularized bone. Patient-related complications such as infection or embolism do not occur in the current experimental setting. These risks are relevant for potential future clinical translation of water-jet and compressed air assisted techniques. Recommended preventive and management measures include sterile closed-loop fluid delivery, pressure and flow control, avoidance of open vessels, effective suction and drainage, and routine monitoring during surgery. Once this laser ablation approach is translated into clinical application, the prevention, monitoring, and management of these potential complications will constitute key safety considerations[61–64]. Future work will therefore focus on fresh, perfused models, quantitative histological and spectroscopic analyzes, and integration with robotic delivery to better assess translational potential.

Methods

Experimental setup

In the ablation experiments, we used two Er:YAG lasers with different intensity distributions: tophat (2940-1500-25, 3 micron Laser Technology) and Gaussian (R7X111C2-ERY, Megawatt tech). Both intensity distributions were validated using a beam profiler (PY-IV-C-A-PRO, Ophiropt). Although the measured profile of the Gaussian laser is multimode (Figure 1), laser with the Gaussian profile refers to this profile throughout the manuscript. An uncoated wedged sapphire window was used to deliver partial energy to the beam profiler, preventing damage from excessive peak power. An energy meter (PE50-DIF-C, Ophiropt) was placed on the beam path after the sapphire window to monitor the incident power in real time, while the reflected beam was measured with the beam profiler.

The experimental setup is demonstrated in Figure 9, where (1) represents both Er:YAG lasers used for bone ablation (laser with tophat intensity distribution: 2940-1500-25, 3 micron Laser Technology, laser with Gaussian intensity distribution: R7X111C2-ERY, Megawatt tech). Three mirrors (2, 4 and 5)(PF10-03-G01, Thorlabs) were placed to redirect the beam. Both lasers have a highly divergent beam (tophat: 12.8 mrad and Gaussian: 7.7 mrad). We used a plano-convex lens (3) with a focal length of 500 mm (LA5464, Thorlabs) for collimation in both experimental setups. The beam was then focused onto the sample by a second plano-convex lens (6). To ensure a consistent beam size at the focal plane for both lasers, two different lenses were selected: 100 mm (LA5817, Thorlabs) for the tophat intensity distribution and 150 mm (LA5012, Thorlabs) for the Gaussian intensity distribution. A coated sapphire window (7) (WG31050-D, Thorlabs) was placed between the sample and the lens to protect against the generated debris and water droplets. The sample (8) is fixed on an XYZ-axis platform (9)(X:KBD101 and DDS050, Thorlabs, Y and Z: 443 and SM50, Newport). The motorized platform was used to move the sample in $\pm X$ direction at a constant speed of 8 mm/s, while the Y and Z-axes were manually adjusted and kept fixed during the experiments.

Laser intensity distribution	Pulse width [µs]	Repetition rate [Hz]	Energy on sample [J]	Beam diameter [mm]	Average fluence [J/cm^2]
tophat	500	10	1.20	1.22	102.7
Gaussian	500	10	1.23	1.25	100.2

Table 2. Parameters comparison of tophat and Gaussian intensity profiles of Er:YAG laser.

In photothermal ablation, irrigation is crucial in obtaining efficient material removal. External irrigation reduces the temperature of the sample and rehydrates bone tissue during the ablation process[38,65]. We used a nozzle (10) (Synova Laser MicroJet Technology) as an irrigation system. The nozzle was placed at an angle of approximately 45° to the sample surface. It generates a 50 µm diameter water jet, which was necessary considering the narrow and deep cut, operating at pressures ranging from 10 bar to 800 bar, and a laminar flow length of >150 mm. Although water cooling helps during the ablation process, debris removal is also very important to keep ablation stable. If irrigation is used and water is not removed well, a liquid layer will form and absorb laser energy, reducing ablation efficiency. Therefore, irrigation should be combined with compressed air or suction, which balances cooling and ablation performance[10,41]. So, a pump system (MP030066, Maximator Schweiz AG), delivering pressurized water through a nozzle, was used. This pump provides a continuous supply of pressurized distilled water with a maximum pressure of 690 bar. At 30 bar, the water flow rate was 4.8 mL/min. In the experiments, we used a Python code to deliver an on-and-off sequence of water flow. The water irrigation nozzle was placed about 100 mm from the sample surface. During deep ablation experiments, to ensure the delivery of water to the deepest point in the cut, we moved the irrigation nozzle about 20 mm forward after the ablation depth reached around 30 mm. The angle between the water and the sample remained unchanged at 45° throughout the movement process. In the meantime, compressed air with a pressure of 15 bar (11) was also used to remove ablation debris and water droplets from the sample surface, with air directed at an angle of approximately 45° to the sample surface, at an angle of approximately 90° to the water jet.

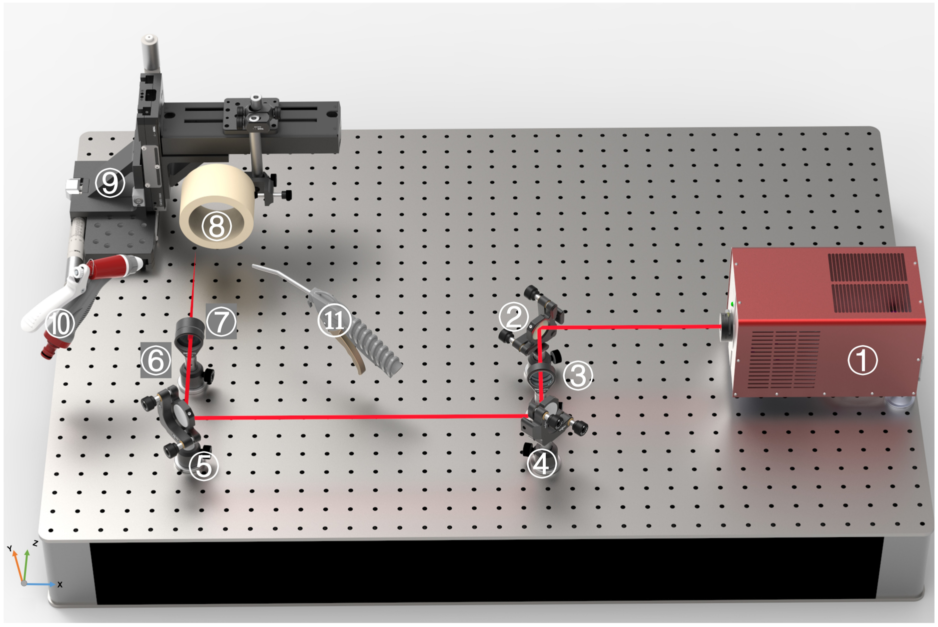

Figure 9. The experimental setup. The system is designed for bone ablation using Er:YAG lasers (1). A plano-convex lens (3) is used for collimation, and mirrors (2, 4, and 5) are placed to redirect the beam to the sample. A plano-convex lens (6) is positioned to focus the beam onto the sample (8). A coated sapphire window (7) protects the optical components from the back. The sample is fixed on an XYZ-axis platform (9). During the ablation experiments, a water jet (10) for cooling and compressed air (11) for debris removal are positioned on either side of the sample. The sample is fixed on an XYZ-axis platform (9) during the experiments.

To isolate the effect of beam shape, all experimental parameters were kept constant, including a shared pulse duration of 500 µs and a repetition rate of 10 Hz. The resultant beam properties on the sample surface were then measured. The tophat distribution had an average energy of 1.20 J and a beam diameter of 1.22 mm, while the Gaussian distribution measured 1.23 J and 1.25 mm, respectively. These settings resulted in an average fluence of 102.7 J/cm^2 and 100.2 J/cm^2, respectively. Table 2 summarizes these parameters.

Material removal rate evaluation

The presence of water molecules, which are the main absorbers of the Er:YAG wavelength, is crucial for initiating micro-explosions and enabling tissue removal. Irrigation systems are commonly used with the Er:YAG laser to both rehydrate the tissue and reduce its temperature. In addition, compressed air is combined with the irrigation system to remove excess water from the tissue, which could otherwise act as a protective layer and absorb the laser energy before it reaches the bone. To investigate the performance of the tophat and Gaussian beams under different experimental conditions, laser ablation was performed on bone samples prepared in varying states. For each energy level (0.4 J to 1.2 J), ablation was performed under three different conditions: (1) dry ablation, also known as direct ablation (without water irrigation and compressed air); (2) water irrigation only for cooling; and (3) a combination of water irrigation and compressed air to remove both debris and excess water while supporting surface cooling. These three conditions were selected based on previously reported studies[38,65].

During each test, the sample was moved horizontally back-and-forth on a motorized stage (KBD101 and DDS050, Thorlabs, with a resolution of ±6.5 µm) and positioned at the focal plane. Each ablation line was approximately 16 mm long, and the sample was moved at a speed of 8 mm/s in a loop motion. Each experiment lasted for 1 min, which was ensured using an optical beam shutter (SH1, Thorlabs). Each set of experiments was repeatedly performed to minimize the impact of experimental and sample deviations. The six ablation lines were performed on three different samples, each with two ablation lines.

After ablation, all lines were scanned using optical coherence tomography (OCT), which measured the material removal rate by providing high-resolution, non-destructive depth measurements. To obtain the ablation depth, a complete OCT scan was performed along the entire ablation region. B-scan images were analyzed with ImageJ (LOCI, University of Wisconsin), and the average depth across the entire scan was defined as the ablation depth.

Depth measurements and bone analysis

Micro-CT scanning

Bone samples were scanned using a Micro-CT system (GE nanotom m, Phoenix) with a resolution of 40 µm and a measurement time of approximately 4 h. The data were then processed using 3D reconstruction software (Datos|x, Phoenix) to obtain a visualized model of the samples.

OCT imaging

To determine the surface removal rate, cross-sectional images were acquired using an OCT system. The OCT system was equipped with an Axsun swept-source laser operating at a central wavelength of 1060 nm, a spectral bandwidth $\Delta\lambda = 100$ nm, and a sweep rate of 100 kHz. The acquired volumetric dataset covered a physical size of 7 x 7 x 3.56 mm, with a volume acquisition rate of 0.37 s^{-1}. The axial and lateral resolutions of the OCT system were 11 µm and 40 µm, respectively. B-scan images were obtained with a lateral field of view of 7 mm and an imaging depth of 3.56 mm in air. For quantitative analysis, the ablation depth and width were extracted through manual segmentation using ImageJ.

SEM

SEM analysis (EM30AX, COXEM) was used to analyze the microstructure of bone samples with a resolution of 5 nm. Since SEM measurements require a low moisture content, the samples were dried in a vacuum desiccator for more than 72 h before testing. Due to the limited working distance and depth of field in SEM, surface ablation was performed for a duration of 10 s on small bone pieces. The samples were then mounted onto the sample stage and secured using conductive tape.

Raman spectroscopy

For Raman spectroscopy testing, bone samples were placed on a Raman spectrometer stage (AIRsight, Shimadzu) and carefully focused under a microscope using a 50 x objective lens. The Raman spectroscopy parameters were as follows: laser wavelength: 785 nm, laser power: 250 mW, exposure time: 10 s, 150 spectra/point, and 3 points for each laser ablation condition. After starting the test, the device recorded Raman spectra acquired from bone samples, which were then used for analysis and comparison.

Theoretical modeling of the ablation process

The Er:YAG laser, operating at 2.94 µm and microsecond pulse width, performs highly efficient photothermal ablation[66] in bone tissue. This mechanism relies on the strong absorption of energy by water and hydroxyapatite, which generates rapid heat and extremely high pressure. The resulting explosive vaporization ejects the tissue. Due to the limited optical penetration depth in bone tissue, the thermal effect is minimal during the ablation process[67], making Er:YAG ablation effectively a 'cold ablation' technique for clinical applications[68].

There are two fundamental models for tissue ablation: the blow-off model[69] and the steady-state model[23]. In both models, ablation occurs only when the energy fluence (energy per unit area) reaches the ablation threshold Φ_{th}. The ablation threshold is defined as the minimum power density required for the removal of the material[23]. Since the Er:YAG laser has a pulse duration in the microsecond range, we focused on the steady-state model.

In the investigated fluence range, the measured single-pulse ablation depth, which is based on the surface material removal rate data (see Figure 3), increases almost linearly with the laser fluence. This shows that the ablation process is in a high-fluence regime, where the ablation efficiency is nearly constant. Therefore, a linear relationship between ablation depth and fluence was used to describe the experimental results. Note that, this linear relationship is inapplicable to low fluence levels.

Based on this linear behavior , the ablation depth l of two intensity distributions under different conditions (dry ablation, with water, and with water and air) was linearly fitted to the incident average fluence using the following equation:

$$l = \frac{dl}{d\Phi_0}\Phi_0 + c, \tag{1}$$

where Φ_0 is the incident average fluence and c is the intercept on the vertical axis.

As shown in Figure 10, the ablation depth of both lasers exhibits a linear relationship under all tested conditions, indicating that the ablation efficiency remains in a steady-state model. Figure 10 is derived from the same ablation experiments as Figure 3 and represents a different evaluation of the same data set. Specifically, Figure 3 shows the material removal rate, which includes both depth and lateral expansion effects, whereas Figure 10 isolates the ablation depth at the crater center. This distinction explains why the removal rate saturates at high fluence, while the ablation depth continues to increase. Since current measurements were performed with relatively high fluence using single-pulse ablation, the evolution of ablation depth under multiple pulses can be predicted using the steady-state model[23]. Table 3 lists the linear fitting parameters for different beam profiles under dry, with water, and with water and air conditions.

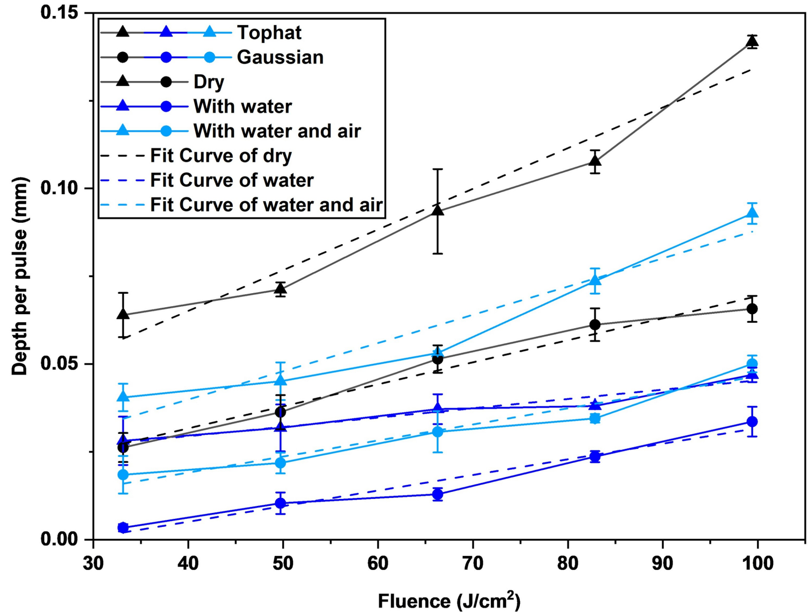

Figure 10. Variation of depth values as a function of incident average fluence in one-pulse ablation under different conditions.

Laser beam	Condition	$dl/d\Phi_0$ [mm^3/J]	c [mm]	R^2
tophat	Dry	0.1160	0.0188	0.9715
	With water	0.0265	0.0189	0.9606
	With water and air	0.0804	0.0090	0.9336
Gaussian	Dry	0.0628	0.0007	0.9514
	With water	0.0444	-0.0127	0.9440
	With water and air	0.0458	0.0008	0.9302

Table 3. Linear fitting parameters (slope ($dl/d\Phi_0$), intercept (c), and coefficient of determination R^2 as shown in Figure 10) of depth per pulse versus fluence for tophat and Gaussian beams under three conditions (dry, with water, and with water and air).

The Gaussian intensity distribution calculations followed the same steps as in Ref.[38]. The fluence Φ_0 is calculated from the incident pulse energy E and the beamwaist w_0 at the focal position. For a Gaussian beam, the fluence at focus was estimated by

$$\Phi_0 = \frac{E}{\pi w_0^2}. \tag{2}$$

To describe the propagation of the focused beam along the optical axis, where λ is the laser wavelength, the evolution of the beam radius $w(z)$ along the propagation direction z can be determined as follows:

$$w(z) = w_0 \sqrt{1 + \left(\frac{z}{z_R}\right)^2}, \tag{3}$$

here, z_R is the Rayleigh range, and w_0 is the beamwaist spotsize of the laser. The Rayleigh range z_R is defined as

$$z_R = \frac{\pi w_0^2}{M^2 \lambda}, \tag{4}$$

the axial variation of the beam radius $w(z)$ is then used to calculate the fluence distribution inside the material. For a Gaussian beam, the fluence distribution is given by

$$\Phi(r,z) = \Phi_0 \left(\frac{w_0}{w(z)}\right)^2 \exp\left(-\frac{2r^2}{w^2(z)}\right), \tag{5}$$

where r is the radial coordinate. Based on parameters which were used in ablation experiments, shown in Table 2, the beam radius at the focal plane w_0 was set to 0.61 mm for the laser with tophat intensity distribution and 0.62 mm for the laser with Gaussian intensity distribution. The operation wavelengths of both lasers were centered at 2.94 µm.

For comparison, a tophat intensity distribution is also considered. In this case, the fluence distribution of the tophat intensity distribution $\Phi(r,z)$ was modified as follows

$$\Phi(r,z) = \begin{cases} \dfrac{E}{\pi w(z)^2}, & 0 \leq r \leq w(z), \\ 0, & r > w(z). \end{cases} \tag{6}$$

here, r is the radial position along the laser beam, E is the laser energy.

The ablation depth of the first pulse was kept in memory, and then we calculated the ablation depth for the second pulse and added to the first ablation depth. Repeating this process for the following pulses allows us to derive the relationship between the number of pulses and the cumulative ablation depth. In our experiments (Figure 5), we obtained the change in the energy efficiency of different lasers as a function of the ablation depth. Therefore, depth-dependent energy efficiency is used in the modeling to make the results more realistic. Finally, based on the laser repetition rate (10 Hz), the relationship between ablation depth and time was obtained.

Sample preparation

The diaphyseal sections of the mature skeletal bovine femurs were harvested, which were purchased from local suppliers. The samples were taken from the middle part of the femur, which consists exclusively of cortical bone and does not include cancellous bone. All samples were ex vivo and used without additional surface treatment. Although the freshness of the samples was unknown, they were stored at $-18\,^{\circ}\mathrm{C}$ immediately after purchase. The bone samples were then thawed from a frozen state at room temperature at least 30 min before testing. This thawing process was necessary to ensure that the samples were in a state conducive to accurate and reliable testing. To further ensure accurate and reliable results, each ablation test was repeated at least three times per specimen.

When multiple ablations were performed on the same sample, we immersed the sample in distilled water at room temperature between each ablation to prevent dehydration. This was performed to reduce the effect of the hydration level of the samples on the experimental results.

Ethics declarations

All experimental samples were obtained from a local supplier. The materials consisted solely of ex vivo animal skeletal tissues, and no live animals or human participants were involved. Therefore, no ethical approval or informed consent was required.

Data Availability

The datasets generated during and/or analyzed during the current study are available from the corresponding author on reasonable request.

References

1. Chen, Z., Wang, C., Jiang, W., Tang, N. & Chen, B. A review on surgical instruments of knee arthroscopic debridement and total hip arthroplasty. *Procedia Cirp* **65**, 291–298, DOI: 10.1016/j.procir.2017.05.001 (2017).
2. Blagova, B., Krastev, D., Krastev, N. & Malinova, L. Tissue changes and tissue reactivity following osteotomy by a conventional rotary device, an ultrasonic unit, and an er:yag laser – a comparative study in humans. *J. Stomatol. Oral Maxillofac. Surg.* **125**, 101750, DOI: 10.1016/j.jormas.2023.101750 (2024).
3. Baek, K. *et al.* A comparative investigation of bone surface after cutting with mechanical tools and er:yag laser. *Lasers Surg. Medicine* **47**, 426–432, DOI: 10.1002/lsm.22352 (2015).
4. Smith, J. O., Wilson, A. J. & Thomas, N. P. Osteotomy around the knee: evolution, principles and results. *Knee Surg Sports Traumatol Arthrosc* **21**, 3–22, DOI: 10.1007/s00167-012-1976-8 (2013).
5. Labanca, M., Azzola, F., Vinci, R. & Rodella, L. F. Piezoelectric surgery: Twenty years of use. *Br. J. Oral Maxillofac. Surg.* **46**, 265–269, DOI: 10.1016/j.bjoms.2007.12.007 (2008).
6. Gleizal, A., Bera, J.-C., Lavandier, B. & Beziat, J.-L. Piezoelectric osteotomy: a new technique for bone surgery—advantages in craniofacial surgery. *Child's Nerv. Syst.* **23**, 509–513, DOI: 10.1007/s00381-006-0250-0 (2007).
7. Aly, L. A. A. Piezoelectric surgery: Applications in oral & maxillofacial surgery. *Futur. Dental J.* **4**, 105–111, DOI: 10.1016/j.fdj.2018.09.002 (2018).
8. den Dunnen, S. & Tuijthof, G. J. M. The influence of water jet diameter and bone structural properties on the efficiency of pure water jet drilling in porcine bone. *Mech. Sci.* **5**, 53–58, DOI: 10.5194/ms-5-53-2014 (2014).

9. den Dunnen, S., Dankelman, J., Kerkhoffs, G. M. & Tuijthof, G. Colliding jets provide depth control for water jetting in bone tissue. *J. Mech. Behav. Biomed. Mater.* **72**, 219–228, DOI: 10.1016/j.jmbbm.2017.05.009 (2017).

10. Stübinger, S. Advances in bone surgery: the er:yag laser in oral surgery and implant dentistry. *Clin. Cosmet. Investig. Dent.* **2**, 47–62, DOI: 10.2147/CCIDE.S8352 (2010).

11. Quest, D., Gayer, C. & Hering, P. Depth measurements of drilled holes in bone by laser triangulation for the field of oral implantology. *J. Appl. Phys.* **111**, 013106, DOI: 10.1063/1.3670000 (2012).

12. Eyrich, G. K. H. Laser-osteotomy induced changes in bone. *Med. Laser Appl.* **20**, 25–36, DOI: 10.1016/j.mla.2005.02.003 (2005).

13. Troedhan, A., Mahmoud, Z., Wainwright, M. & Khamis, M. Cutting bone with drills, burs, lasers and piezotomes: A comprehensive systematic review and recommendations for the clinician. *Int. J. Oral Craniofacial Sci.* **3**, 020–033, DOI: 10.17352/2455-4634.000028 (2017).

14. Tillotson, C. L., Rosenberg, A. E. & Rosenthal, D. I. Controlled thermal injury of bone: Report of a percutaneous technique using radiofrequency electrode and generator. *Investig. Radiol.* **24**, 888, DOI: 10.1097/00004424-198911000-00009 (1989).

15. Hamidi, A. *et al.* Multimodal feedback systems for smart laser osteotomy: Depth control and tissue differentiation. *Lasers Surg. Medicine* **55**, 900–911, DOI: 10.1002/lsm.23732 (2023).

16. Gunaratne, R. *et al.* Wavelength weightings in machine learning for ovine joint tissue differentiation using diffuse reflectance spectroscopy (drs). *Biomed. Opt. Express* **11**, 5122–5138, DOI: 10.1364/BOE.397593 (2020).

17. Hamidi, A. *et al.* Long-range optical coherence tomography with extended depth-of-focus: a visual feedback system for smart laser osteotomy. *Biomed. Opt. Express* **12**, 2118–2133, DOI: 10.1364/BOE.414300 (2021).

18. Ashok, P. C., Giardini, M. E., Dholakia, K. & Sibbett, W. A raman spectroscopy bio-sensor for tissue discrimination in surgical robotics. *J. Biophotonics* **7**, 103–109, DOI: 10.1002/jbio.201300034 (2014).

19. Weiner, S. & Wagner, H. D. The material bone: Structure-mechanical function relations. *Annu. Rev. Mater. Sci.* **28**, 271–298, DOI: 10.1146/annurev.matsci.28.1.271 (1998).

20. Liu, Y. & Niemz, M. Ablation of femoral bone with femtosecond laser pulses—a feasibility study. *Lasers Med. Sci.* **22**, 171–174, DOI: 10.1007/s10103-006-0424-8 (2007).

21. Ivanenko, M., Werner, M., Afilal, S., Klasing, M. & Hering, P. Ablation of hard bone tissue with pulsed CO2 lasers. *Med. Laser Appl.* **20**, 13–23, DOI: 10.1016/j.mla.2005.02.007 (2005).

22. Kim, K., Kim, I. S., Cho, T. H., Seo, Y.-K. & Hwang, S. J. High-intensity nd:yag laser accelerates bone regeneration in calvarial defect models. *J. Tissue Eng. Regen. Medicine* **9**, 943–951, DOI: 10.1002/term.1845 (2015).

23. Vogel, A. & Venugopalan, V. Mechanisms of pulsed laser ablation of biological tissues. *Chem. Rev.* **103**, 577–644, DOI: 10.1021/cr010379n (2003).

24. Beltran Bernal, L. M. *Laser and wave-guides system for endoscopic/fiberscopic laser surgery*. Ph.d. thesis, University of Basel, Basel, Switzerland (2021).

25. Liaw, L. Mid-infrared erbium:yag laser ablation of bone: The effect of laser osteotomy on bone healing. *Lasers Surg. Medicine* **9**, 409–417, DOI: 10.1002/lsm.1900090409 (1989).

26. Yoshino, T. *et al.* Long-term histologic analysis of bone tissue alteration and healing following er:yag laser irradiation compared to electrosurgery. *J. Periodontol.* **80**, 82–92, DOI: 10.1902/jop.2009.080097 (2009).

27. Deep, K. & Picard, F. A detailed analysis of time taken in robotic surgery for total knee replacement arthroplasty and comparison with computer assisted navigation in total knee replacement arthroplasty. In *EPiC Series in Health Sciences, Volume 4: Proceedings of CAOS 2020*, 56–58, DOI: 10.29007/65qr (2020).

28. Hafez, M. A., Chelule, K. L., Seedhom, B. B. & Sherman, K. P. Computer-assisted total knee arthroplasty using patient-specific templating. *Clin. Orthop. Relat. Res.* **444**, 184–192, DOI: 10.1097/01.blo.0000201148.06454.ef (2006).

29. Graceffa, A., Indelli, P. F., Basnett, K. & Marcucci, M. Analysis of differences in bone removal during femoral box osteotomy for primary total knee arthroplasty. *Joints* **2**, 76–80, DOI: 10.11138/jts/2014.2.2.076 (2014).

30. Hampp, E. L. *et al.* Robotic-arm assisted total knee arthroplasty demonstrated greater accuracy and precision to plan compared with manual techniques. *J. Knee Surg.* **32**, 239–250, DOI: 10.1055/s-0038-1641729 (2019).

31. Schnurr, C., Csécsei, G., Nessler, J., Eysel, P. & König, D. P. How much tibial resection is required in total knee arthroplasty? *Int. Orthop.* **35**, 989–994, DOI: 10.1007/s00264-010-1025-5 (2011).

32. Ran, T. *et al.* Ultra-pulsed CO2 laser osteotomy: A new method for the bone preparation of total knee arthroplasty. *Front. Bioeng. Biotechnol.* **10**, DOI: 10.3389/fbioe.2022.858862 (2022).

33. Ran, T. Basic research on application of ultra-pulsed co2 laser osteotomy in total knee arthroplasty. *Thesis* (2022).

34. Howell, S. M., Nedopil, A. J. & Hull, M. L. Negligible effect of surgeon experience on the accuracy and time to perform unrestricted caliper verified kinematically aligned tka with manual instruments. *Knee Surgery, Sports Traumatol. Arthrosc.* **30**, 2966–2974, DOI: 10.1007/s00167-022-06939-y (2022).

35. Cetin, C. *et al.* Bone ablation performance of a ho:yag laser. In *Optical Interactions with Tissue and Cells XXXIV*, vol. 12377, 46–48, DOI: 10.1117/12.2647703 (SPIE, 2023).

36. Mishra, B. *et al.* Ultrafast laser bone ablation towards high surgical speeds and clinically relevant operation times for spine surgeries. *Biomed. Opt. Express* **16**, 1871–1886, DOI: 10.1364/BOE.555846 (2025).

37. Zhang, J., Guan, K., Zhang, Z. & Guan, Y. In vitro evaluation of ultrafast laser drilling large-size holes on sheepshank bone. *Opt. Express* **28**, 25528–25544, DOI: 10.1364/OE.396727 (2020).

38. Bernal, L. M. B. *et al.* Optimizing deep bone ablation by means of a microsecond er:yag laser and a novel water microjet irrigation system. *Biomed. Opt. Express* **11**, 7253–7272, DOI: 10.1364/BOE.408914 (2020).

39. Seymen, G., Turgut, Z., Berk, G. & Bodur, A. Implant bed preparation with an er,cr:ysgg laser using stereolithographic surgical guide. *J. Lasers Med. Sci.* **4**, 25–32, DOI: 10.3923/jlms.2013.25.32 (2013).

40. Ji, L. *et al.* Laser rapid drilling of bone tissue in minimizing thermal injury and debris towards orthopedic surgery. *Mater. & Des.* **220**, 110895, DOI: 10.1016/j.matdes.2022.110895 (2022).

41. Stübinger, S., Ghanaati, S., Saldamli, B., Kirkpatrick, C. J. & Sader, R. Er:yag laser osteotomy: Preliminary clinical and histological results of a new technique for contact-free bone surgery. *Eur. Surg. Res.* **42**, 150–156, DOI: 10.1159/000197216 (2009).

42. Pandurić, D. G. *et al.* Comparison of er:yag laser and surgical drill for osteotomy in oral surgery: An experimental study. *J. Oral Maxillofac. Surg.* **70**, 2515–2521, DOI: 10.1016/j.joms.2012.06.192 (2012).

43. de Mello, E. D. A. *et al.* Comparative histological analysis of bone healing of standardized bone defects performed with the er:yag laser and steel burs. *Lasers Med. Sci.* **23**, 253–260, DOI: 10.1007/s10103-007-0475-5 (2008).

44. Stock, K., Diebolder, R., Hausladen, F. & Hibst, R. Efficient bone cutting with the novel diode pumped er:yag laser system: in vitro investigation and optimization of the treatment parameters. In *Photonic Therapeutics and Diagnostics X*, vol. 8926, 452–461, DOI: 10.1117/12.2039648 (SPIE, 2014).

45. Pourzarandian, A. *et al.* Histological and tem examination of early stages of bone healing after er:yag laser irradiation. *Photomed. Laser Surg.* **22**, 342–350, DOI: 10.1089/pho.2004.22.342 (2004).

46. Köhnke, R. *et al.* Performance and safety evaluation of a cold ablation robot-guided laser osteotome (carlo) in 28 midface osteotomies. *Sci. Reports* **14**, 27160, DOI: 10.1038/s41598-024-68557-7 (2024).

47. Holzinger, D. *et al.* First-in-man application of a cold ablation robot guided laser osteotome in midface osteotomies. *J. Cranio-Maxillofacial Surg.* **49**, 531–537, DOI: 10.1016/j.jcms.2021.01.007 (2021).

48. Shekarriz, H. *et al.* Hydro-jet-assisted laparoscopic cholecystectomy: a prospective randomized clinical study. *Surgery* **133**, 635–640, DOI: 10.1067/msy.2003.155 (2003).

49. den Dunnen, S., Dankelman, J., Kerkhoffs, G. M. M. J. & Tuijthof, G. J. M. How do jet time, pressure and bone volume fraction influence the drilling depth when waterjet drilling in porcine bone? *J. Mech. Behav. Biomed. Mater.* **62**, 495–503, DOI: 10.1016/j.jmbbm.2016.05.026 (2016).

50. Absolonová, K., Dobisíková, M., Beran, M., Zocová, J. & Velemínský, P. The temperature of cremation and its effect on the microstructure of the human rib compact bone. *Anthropol. Anzeiger* **69**, 439–460, DOI: 10.1127/0003-5548/2012/0213 (2012).

51. Gross, K. A. & Berndt, C. C. Thermal processing of hydroxyapatite for coating production. *J. Biomed. Mater. Res.* **39**, 580–587, DOI: 10.1002/(SICI)1097-4636(19980315)39:4<580::AID\protect\unhbox\voidb@x\hbox{-}JBM12>3.0.CO;2\protect\unhbox\voidb@x\hbox{-}B (1998).

52. Pantawane, M. V. *et al.* Thermal assessment of ex vivo laser ablation of cortical bone. *ACS Biomater. Sci. & Eng.* **6**, 2415–2426, DOI: 10.1021/acsbiomaterials.9b01559 (2020).

53. Ben-Nissan, B. *Advances in Calcium Phosphate Biomaterials*, vol. 2 (Springer Berlin Heidelberg, Berlin, Heidelberg, 2014).

54. Rapp, L. *et al.* Investigation of laser wavelength effect on the ablation of enamel and dentin using femtosecond laser pulses. *Sci. Reports* **13**, 20156, DOI: 10.1038/s41598-023-47551-5 (2023).

55. Geraldes, C. F. G. C. Introduction to infrared and raman-based biomedical molecular imaging and comparison with other modalities. *Molecules* **25**, 5547, DOI: 10.3390/molecules25235547 (2020).

56. Nahen, K. & Vogel, A. Plume dynamics and shielding by the ablation plume during er:yag laser ablation. *J. Biomed. Opt.* **7**, 165 (2002).

57. Kang, H. W., Lee, H., Chen, S. & Welch, A. J. Enhancement of bovine bone ablation assisted by a transparent liquid layer on a target surface. *IEEE J. Quantum Electron.* **42**, 633–642 (2006).

58. McCaughey, R. G., Sun, H., Rothholtz, V. S., Juhasz, T. & Wong, B. J. F. Femtosecond laser ablation of the stapes. *J. Biomed. Opt.* **14**, 024040 (2009).

59. Nguendon Kenhagho, H. *et al.* Characterization of ablated bone and muscle for long-pulsed laser ablation in dry and wet conditions. *Mater. (Basel)* **12**, 1338 (2019).

60. Stock, K., Hibst, R. & Keller, U. Comparison of er:yag and er:ysgg laser ablation of dental hard tissues. *Proc. SPIE* **3192**, 88–95, DOI: 10.1117/12.297864 (1997).

61. Mirski, M. A., Lele, A. V., Fitzsimmons, L. & Toung, T. J. K. Diagnosis and treatment of vascular air embolism. *New Engl. J. Medicine* **356**, 789–799, DOI: 10.1056/NEJMra070569 (2007).

62. Svenarud, P., Persson, M. & van der Linden, J. Effect of carbon dioxide insufflation on the number and behavior of gas emboli. *Circulation* **109**, 834–839, DOI: 10.1161/01.CIR.0000118501.44474.83 (2004).

63. Granick, M. S., Boykin, J. V., Gamelli, R. L., Schultz, G. S. & Tenenhaus, M. Versajet hydrosurgery system: a new tool for wound debridement. *Plast. Reconstr. Surg.* **117**, 2195–2200, DOI: 10.1097/01.prs.0000209963.52367.5f (2006).

64. Manner, M., Aydin, A., Schmidt, M. *et al.* Air entrainment during laparoscopy using a valveless trocar system. *Surg. Endosc.* **29**, 2311–2318, DOI: 10.1007/s00464-014-3914-4 (2015).

65. Bernal, L. M. B. *et al.* Performance of er:yag laser ablation of hard bone under different irrigation water cooling conditions. In *Optical Interactions with Tissue and Cells XXIX*, vol. 10492, 43–49, DOI: 10.1117/12.2290929 (SPIE, 2018).

66. Noginov, M. A., Sarkisyan, G. K., Smirnov, V. A., Umyskov, A. F. & Shcherbakov, I. A. Experimental observation of the nonadditivity of various mechanisms of population inversion of the $^4i_{11/2} \to {}^4i_{13/2}$ transition of the Er^{3+} ion in a YSGG:Cr^{3+}:Er^{3+} crystal. *Sov. J. Quantum Electron.* **20**, 638, DOI: 10.1070/QE1990v020n06ABEH006666 (1990).

67. Aoki, A. *et al.* Current status of er:yag laser in periodontal surgery. *Jpn. Dental Sci. Rev.* **60**, 1–14, DOI: 10.1016/j.jdsr.2023.11.002 (2024).

68. Honigmann, P. *et al.* Cold ablation robot-guided laser osteotomy in hand, wrist and forearm surgery—a feasibility study. *The Int. J. Med. Robotics Comput. Assist. Surg.* **18**, e2438, DOI: 10.1002/rcs.2438 (2022).

69. Welch, A. J. *Optical-Thermal Response of Laser-Irradiated Tissue* (Springer Netherlands, Dordrecht, 2011).

Funding

This project was co-funded by the Werner Siemens Foundation as part of the MIRACLE project and Innosuisse – Swiss Innovation Agency under project number 112.465 IP-LS, titled LASER-Blade.

Author Contributions

Mr. Mingyi Liu performed the experimental study, performed the analyzes throughout the study, and prepared the manuscript.
Dr. Arsham Hamidi supported and advised on data analysis and manuscript organization and particularly contributed to the ablation profile investigation approach.
Dr. Dunia Blaser participated in the supervision of the study and the revision of the manuscript.
Dr. Darren Wilson supervised the project timeline and provided significant input on the experimental methods.
Dr. Kenneth Garcia contributed to the conceptual study and provided input in the study planning.
Prof. Dr. Niklaus F. Friederich provided insight on the medical expectations and contributed to the conceptualization.
Prof. Dr. Georg Rauter supported the data analysis and revised the paper.
Prof. Dr. Philippe C. Cattin contributed to the conceptualization of the study, reviewed the data analysis, and contributed to the organization of the manuscript.
Dr. Ferda Canbaz conceptualized the research project and provided guidance on the methodology and overall research direction.

She has contributed to data analysis, manuscript organization, and preparation. All authors reviewed and approved the final manuscript. The authors declare no conflict of interest.

Acknowledgments

The authors acknowledge the contributions of Dr. Georg Schulz for CT measurements, training, and analysis. Prof. Dr. Bert Müller and Dr. Iwan Jerjen for SEM imaging, sample preparation, measurement training, and data analysis. Special thanks to Prof. Elia Marin from Kyoto Institute of Technology for his feedback regarding the Raman spectra. Thanks to Leya Pauly and Vinamrata Bhardwaj for their careful proofreading of the sentences. The manuscript was revised using AI tools such as Grammarly for grammar correction.